

When do microswimmers exit the Stokes regime?

KRISTINA PICKL¹ *, JAYANT PANDE² *, HARALD KÖSTLER¹, ANA-SUNČANA SMITH^{2,3} (a) and ULRICH RÜDE¹

¹ *Lehrstuhl für Systemsimulation, Friedrich-Alexander-Universität Erlangen-Nürnberg, Erlangen, Germany*

² *EAM Cluster of Excellence, Friedrich-Alexander-Universität Erlangen-Nürnberg, Erlangen, Germany*

² *PULS group, Department of Physics, Friedrich-Alexander-Universität Erlangen-Nürnberg, Erlangen, Germany*

³ *Division of Physical Chemistry, Ruđer Bošković Institute, Zagreb, Croatia*

* *These authors contributed equally to this work.*

PACS 47.63.Gd – Swimming microorganisms

PACS 47.11.-j – Computational methods in fluid dynamics

PACS 87.85.Tu – Modeling biomedical systems

Abstract – We compare fully-resolved, 3D lattice Boltzmann (LB) simulations of a three sphere microswimmer to analytical calculations, and show thereby that (i) LB simulations reproduce the motion very well in the Stokes regime, and (ii) the swimmer exits this regime at Reynolds numbers $Re \sim 10^{-2}$, significantly lower than previously realised. Below this Re value Stokesian theory describes the motion accurately, but fails above it due to inertial effects. In the latter case, the swimmer’s relaxation matches that of an underdamped harmonic oscillator, and this specifies its effective hydrodynamic radius in a narrow Re range, as we show by calculating the radius analytically. The method can be used to determine the limit of the Stokes regime and the effective radius for a general mechanical microswimmer.

Introduction. – The motion of microswimmers, whether natural ones like *E. coli* [1] and *C. reinhardtii* [2] or artificial ones like various proposed micro-machines [3–7], is dominated by the viscous forces exerted by the surrounding fluid, with the inertia of the swimmers playing practically no role. For these organisms the Reynolds number (Re) is typically very small, usually 10^{-2} or smaller. Because of this, a common approach in the literature to model their motion is to assume that the Re vanishes [8–12]. In this limit the non-linear terms in the Navier-Stokes equation for the fluid flow can be eliminated, resulting in the Stokes equation, which makes the analysis of the motion much easier [9]. The swimmers are then said to be in the “Stokes regime”.

Larger organisms such as small insects swim in what may be termed the “intermediate regime”, at which both the viscous forces and the inertial forces are important in directing the motion [13]. Their Reynolds numbers typically range between 1 and a few hundred. Finally, organisms on the scale of meters, such as large fish, swim at $Re \gtrsim 10^3$, where the inertial forces dominate the motion, and the coasting of the swimmer during the non-active part of each cycle is an integral part of the swimming strat-

egy [14]. This is the domain of the “non-Stokes regime”.

The above demarcation of the three regimes is only loosely defined, with the specific details of a swimmer controlling its Reynolds number as well as the importance of inertial effects in determining its motion. In practice $Re < 1$ is often taken to be a sufficient condition for assuming the Stokes regime, but the validity of such an assumption is not established. Moreover, inherently non-Stokesian methods such as lattice Boltzmann (LB) simulations are often used to simulate microswimmers with $Re < 1$, and any inertial effects if present in the simulation are typically ignored in the analysis.

In this work we study the limits of the Stokes regime for microswimmers and the suitability of using LB simulations within and beyond this regime. We adopt as a model the popular three-sphere microswimmer of Najafi and Golestanian [4], modified to allow consideration of the forces driving the motion. We show that for sufficiently low driving forces and sphere masses and consequently small Re , LB simulations reproduce to a high degree of accuracy the swimmer motion predicted by purely Stokesian theory. As Re becomes larger than 10^{-2} , Stokesian theory fails and the swimmer enters the intermediate regime, where its motion is characterised by inertial coasting in accordance with the Stokes drag law as well as the expo-

(a)E-mail: smith@physik.fau.de

mental oscillation of an underdamped harmonic oscillator. The damping constant for this motion depends on the effective hydrodynamic radius of the swimmer. This fact can be used to identify the intermediate regime and find the effective radius for a general mechanical microswimmer driven by elastic shape changes.

For the three-sphere swimmer, the intermediate regime is narrow, with its upper limit being at $Re \sim 5 \times 10^{-2}$. Above this Re value, the coasting exhibited by the swimmer is stronger than that predicted using the Stokes force law and the swimmer enters the inertia-dominated non-Stokes regime. The limit of the Stokes regime as found by us is therefore considerably smaller than the low Re limit of $Re < 0.5$ for an isolated three-sphere swimmer suggested by Pooley and Yeomans using LB simulations in 2D [15].

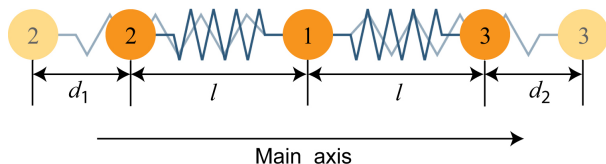


Fig. 1: Three-sphere swimmer model, based on [4].

Swimmer model. – Our swimmer, based on the Najafi-Golestanian design [4], consists of three rigid spheres of equal masses m and radii r connected by two linear springs of equal stiffness constants k and mean rest lengths l . In the simulations, additionally, we include angular springs of high stiffness constants to ensure linear and rotational alignment of the swimmer [16]. Time-irreversibility in the stroke, as required by the Scallop Theorem for net propulsion at zero Reynolds number [3], is achieved via the sinusoidal driving forces

$$F_{d_1}(t) = -(F_{d_2}(t) + F_{d_3}(t)), \quad (1)$$

$$F_{d_2}(t) = -a \sin(\omega t), \quad \text{and} \quad (2)$$

$$F_{d_3}(t) = b \sin(\omega t + \alpha), \quad \text{for } t \geq (\pi - \alpha) / \omega, \quad (3)$$

that are applied to the centers of mass of the spheres along the main axis of the swimmer, the x -axis. The parameters a and b denote the amplitudes of the sinusoidal forces, ω is the force frequency, T is the cycle period (so that $T = 2\pi/\omega$), α is the relative phase shift in the forces and t is the instantaneous time. The force F_{d_3} on the right sphere is kept zero for the first $(\pi - \alpha) / \omega$ time steps, so that it starts continuously from a value of zero as that aids in the stability of simulations; this has no bearing on the model itself. Due to Eq. (1) the criterion of force neutrality is always satisfied. As a result of the forces, the trailing and leading arms perform sinusoidal motion with oscillation amplitudes d_1 and d_2 , respectively (Fig. 1).

Simulation framework. – The simulation system consists of two parts, the parallel software framework

WALBERLA [17–19] for simulating the fluid, and the rigid body engine *pe* [20] for the bodies within it.

WALBERLA is based on the lattice Boltzmann method (LBM) [21, 22] and uses a D3Q19 model [23] for three-dimensional space discretisation employing 19 particle distribution functions (PDFs) per lattice site. For the collision operator, Ginzburg’s two-relaxation time model [24] is applied, which splits the PDFs, the used incompressible equilibrium distribution function, and the relaxation parameter into symmetric and antisymmetric parts. For the simulations, the best accuracy at the solid walls is achieved with the symmetric relaxation parameter set to $1/\tau$ and the antisymmetric one set to $8(2 - 1/\tau)/(8 - 1/\tau)$ [24], where τ denotes the relaxation time. The software utilizes the message passing interface (MPI) and is optimized for scalable and efficient execution on the fastest supercomputers available [25].

The massively parallel rigid body engine *pe* [20] handles the dynamics of the bodies using Newton’s equations of motion, and includes mechanisms for resolving frictional rigid body collisions and modelling external forces like gravity or the sinusoidal forces driving the swimmer. Potential contacts are handled in this work using the parallel Discrete Element Method (DEM) [26]. In addition to these soft-contact models it also supports, *e.g.*, a contact resolution based on hard-contact models [27]. The algorithm is augmented with an MPI communication strategy that can handle general pairwise spring-damper systems [16]. To avoid problems resulting from non-local communication among processes resulting from extended springs, communication is restricted to those pairs of processes on which objects interact. Global communication is avoided since it might lead to a deterioration of parallel performance and scalability on modern supercomputers.

The interactions between the swimmer and the fluid, as well as between different bodies within the swimmer, are modelled by a four-way coupling scheme [16, 28, 29]. The rigid bodies of the swimmer overlap with the cells of the LBM grid and are marked as obstacles within the fluid. Those that interface to the fluid are specified to have a moving boundary condition [30–32]. The fluid couples to a rigid body via the momentum exchange method [30, 31, 33] that takes into account the instantaneously acting hydrodynamic forces from the fluid on the rigid body. A detailed description of the algorithms and methods used in the simulation systems can be found in Pickl *et al.* [16, 28].

Stokes regime: velocity and stroke. – To first test the suitability of the LBM simulation system to reproduce swimming within the Stokes regime, we compare the simulation results with purely Stokesian theory. We have described this theory in previous work [34, 35], where we have determined the velocity of the swimmer by considering the effect on each sphere of the different forces it faces, these being the spring forces, the driving forces and the hydrodynamic forces. For small driving forces, the oscillations of the spheres are small too, and one ob-

tains a coupled system of ordinary differential equations for the sphere positions as functions of time, due to the linear velocity-force relationship in Stokes flow. This system is solved in a perturbative manner with the oscillation of the swimmer arms being the variable of perturbation, and this leads to a swimming velocity given by (in the notation employed in this paper) [35]

$$u_{\text{force}} = \frac{7r [2(a^2 - b^2)\kappa r - ab(\kappa^2 + 12r^2)\sin\alpha]}{24l^2\pi^2\nu^2\rho^2\omega(\kappa^4 + 40\kappa^2r^2 + 144r^4)}. \quad (4)$$

Here u_{force} denotes the swimming velocity calculated using the forces acting upon the swimmer, ν is the kinematic viscosity of the fluid, ρ is its density, and κ is a constant defined for convenience as $\kappa = k/(\pi\nu\rho\omega)$. This calculation assumes that there is no slip between the spheres and the fluid, and that the distances between the spheres are much larger than the other length scales in the problem.

In response to the driving forces, the swimming stroke induced is sinusoidal, and can be expressed as

$$\begin{aligned} L_1(t) &= l + d_1 \cos(\omega t + \delta_1), \\ L_2(t) &= l + d_2 \cos(\omega t + \delta_2), \end{aligned} \quad (5)$$

where L_i is the instantaneous length of the i^{th} arm, and d_i and δ_i are the amplitude and the phase of its oscillation. Once this form of the swimming stroke is adopted, and the earlier-mentioned conditions of no fluid slip, large sphere separations and small arm-length oscillations are assumed, then the swimmer's velocity can be written as [36]

$$u_{\text{stroke}} = Gd_1d_2\omega \sin(\delta_1 - \delta_2). \quad (6)$$

Here u_{stroke} is the swimming velocity (with the subscript referring to the stroke-dependence of its calculation), and G is a geometrical constant which for equal sphere radii r and equal mean arm-lengths l is given by $G = 7r/(24l^2)$.

The two approaches of finding the swimming velocity—*i.e.* assuming known driving forces and known strokes—may be reconciled by determining the various stroke parameters for the assumed force protocol, and then using the now-known strokes to find the velocity as in Eq. (6). The stroke parameters are found to be

$$\begin{aligned} d_1 &= \sqrt{\frac{a^2\kappa^2 + 4r^2 [4a^2 + b^2 - 4ab \cos \alpha] + 4ab\kappa r \sin \alpha}{\pi^2\nu^2\rho^2\omega^2 (\kappa^4 + 40\kappa^2r^2 + 144r^4)}}, \\ d_2 &= \sqrt{\frac{b^2\kappa^2 + 4r^2 [a^2 + 4b^2 - 4ab \cos \alpha] - 4ab\kappa r \sin \alpha}{\pi^2\nu^2\rho^2\omega^2 (\kappa^4 + 40\kappa^2r^2 + 144r^4)}}. \end{aligned} \quad (7)$$

The stroke phase difference $\sin(\delta_1 - \delta_2)$ is presented in the Supplementary Information (SI) due to the length of the expression involved.

Recasting now the stroke-based velocity form of Eq. (6) into the force-based one of Eq. (4), we find

$$u_{\text{stroke}} \approx \frac{7(4l - 3r)(4l - 7r)}{4l(28l - 45r)} u_{\text{force}}. \quad (8)$$

Clearly, to the lowest order in r/l , the two velocities match each other perfectly.

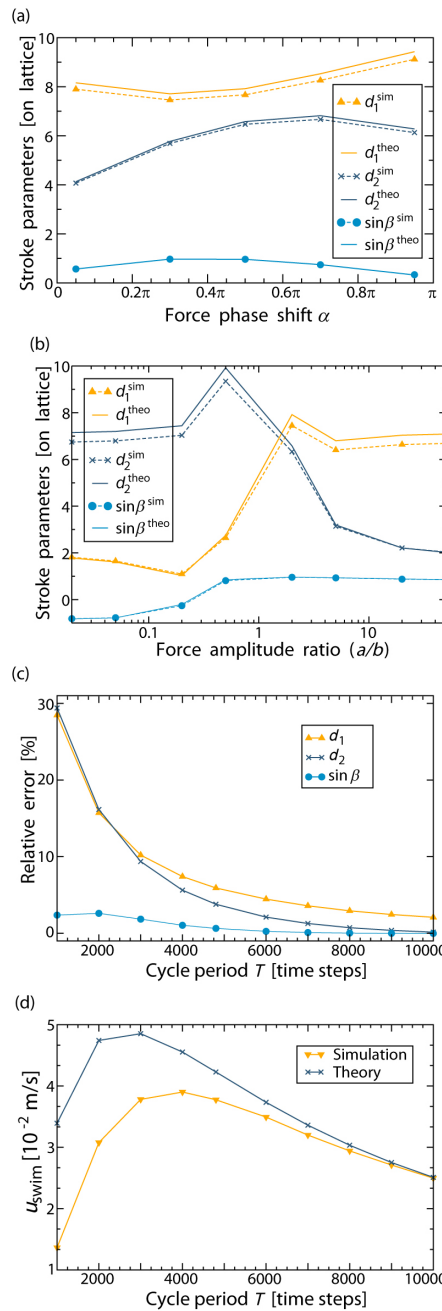


Fig. 2: Dependence of the stroke parameters on (a) the force phase shift α , (b) the force amplitude ratio a/b , and (c) the cycle period T ; and (d) comparison of velocity from theory and simulations for different cycle periods. The superscripts ‘sim’ and ‘theory’ refer to simulations and theory, respectively.

Comparison to simulation results. We compare the above theory with simulations using the WALBERLA-*pe* framework. In all the simulations, the fluid has a kinematic viscosity of $\nu = 7.36 \times 10^{-5} \text{ m}^2/\text{s}$ and a density of $\rho = 1.36 \times 10^3 \text{ kg/m}^3$. The relaxation time is set to $\tau = 1.5$, and the lattice resolution to 10^{-6} m . The spring stiffness is $k = 2.3 \text{ kg/s}^2$, and the mass of each sphere is $m = 5.44 \times 10^{-13} \text{ kg}$ while its radius is $r = 4 \times 10^{-6} \text{ m}$.

Each arm has a rest length of $l = 2.0 \times 10^{-5}$ m. The simulations are carried out in a box of size $(x \times y \times z) = (1200 \times 800 \times 800)$ lattice cells, and six full swimming cycles are performed in total to ensure that the steady state is reached. The other parameters in the different simulations are detailed in the SI (Table 1).

Figs. 2 (a) and (b) show a comparison of the stroke parameter values from theory and from simulations for increasing values of the force phase shift α and the force amplitude ratio a/b , respectively, for a cycle period of 4800 time steps. The errors are less than 6% in both cases. If the cycle period is increased, the errors become even smaller (Fig. 2 (c)), since the accuracy of the force resolution in the simulations increases with the cycle period.

Comparison of the swimmer velocity from theory and simulations shows good agreement as well (Fig. 2 (d)), with the relative errors again going down as the cycle period increases (to 0.5% for a cycle period of 10000). This shows the suitability and the robustness of the LBM system to simulate Stokesian swimmers. Note that LBM is subject to unavoidable boundary effects and discretization errors; these however prove to be small enough to not affect the results significantly.

Swimmers beyond the Stokes regime. – We now focus on finding the Reynolds numbers at which the Stokes regime is surpassed by our swimmers, and for this make them heavier and faster. The radius of each sphere in the simulations is increased to 6×10^{-6} m, its mass to 5.44×10^{-11} kg, and the rest length of each arm to 3.2×10^{-5} m. The cycle period is increased to 8000 time steps to aid simulation accuracy. The phase shift α is set to 0.5π .

We run a series of ten simulations where the equal driving force amplitudes increase successively from a value of 3.71×10^{-6} N to one of 3.71×10^{-5} N, in multiples of the smaller value. The largest allowed force amplitude is set by the requirement of keeping a minimum distance of one lattice cell between any two spheres at all times. This is important because at smaller distances, lubrication correction forces are switched on in the simulation system, and these are not included in the theoretical model.

We find that the earlier-described theory predicts the correct swimmer velocities only for low driving force amplitudes, and diverges from the simulations as the forces increase (Fig. 3). This matches the expectation of a continuous transition from the Stokes regime (Fig. 3, left blue region) to the non-Stokes one (Fig. 3, right yellow region). In between lies an intermediate regime (Fig. 3, middle pink region) where the transition occurs. In the next section, we locate this transition more precisely.

Swimmer relaxation. The swimmer can be viewed as a system of connected harmonic oscillators, which are coupled through both the middle sphere and the surrounding fluid, as well as damped by the fluid. Since the drag force is dominant in Stokes flow, we assume that the Stokes and the non-Stokes regimes are characterised by overdamping and underdamping, respectively, in the motion of this os-

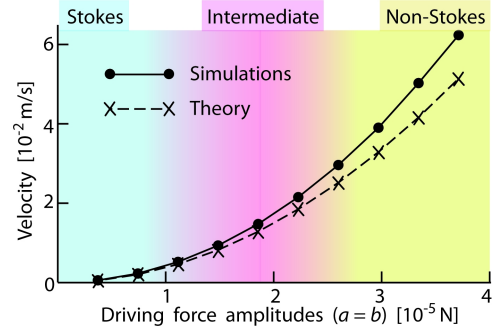


Fig. 3: Velocity of swimmer for different force amplitudes, from simulations and theory.

cillator system. For an underdamped driven harmonic oscillator, the trajectory is given by

$$x(t) = x_0 e^{-\gamma t} \cos(\omega_r t - \alpha_r), \quad (9)$$

where x_0 is the maximum amplitude, γ is the damping constant, and ω_r and α_r are constants of oscillation. For underdamped motion of a coupled system such as ours, and of any mechanical microswimmer in general, it is difficult to specify the different parameters in Eq. (9), yet the damping coefficient γ may still be identified. To do this, consider the swimmer's relaxation from an initially steady state when the driving forces are switched off. In the steady state, the swimmer faces the Stokes drag force $F_{St} = -6\pi\eta r_{eff}u$ where r_{eff} is its effective hydrodynamic radius. When the driving forces vanish, then the body stops instantly if inertial effects are discounted, but in the presence of inertia the body exhibits coasting, and its velocity decreases continuously as

$$\begin{aligned} F_{St} &= mdu/dt = -6\pi\eta r_{eff}u. \\ \Rightarrow u &= Ce^{-\gamma t}, \text{ with } \gamma = \frac{6\pi\eta r_{eff}}{m} \text{ and } C \text{ a constant.} \end{aligned} \quad (10)$$

Due to the use of the Stokes drag force F_{St} in obtaining γ , Eq. (9) with said γ describes the relaxation only in the intermediate regime between the Stokes and the non-Stokes ones. Therefore, by fitting the relaxation curve of the swimmer with Eq. (9), the intermediate regime can be identified. This can then also be used to determine the swimmer's effective hydrodynamic radius r_{eff} , by using Eq. (10) to find r_{eff} once γ has been identified from the fit to Eq. (9). This procedure can be used for other mechanical microswimmers such as in [3, 6] which can be viewed as oscillators.

Swimmer effective radius. In order to check the validity of the method, we first find the effective hydrodynamic radius r_{eff} for our swimmer from theory. For negligibly small oscillation amplitudes, *i.e.* to the zeroth order in d_i/l_j , the r_{eff} for the swimmer over a cycle is the same as that of the equilibrium configuration moving rigidly with a constant velocity. Such a rigid configuration is obtained for our swimmer when the driving forces on the

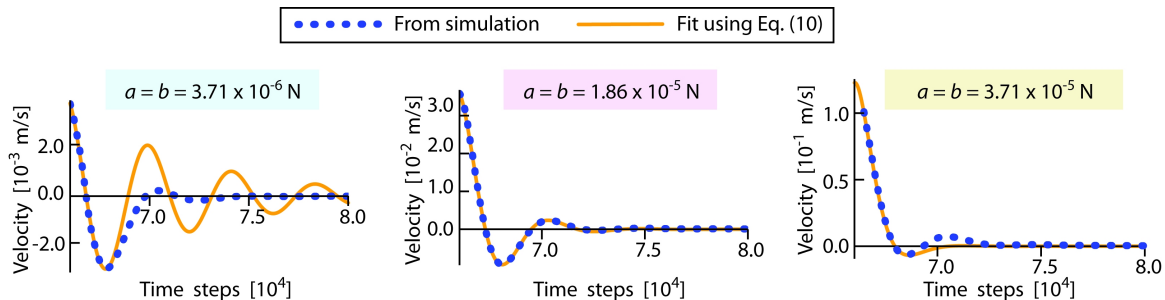


Fig. 4: Relaxation of swimmer for different driving force amplitudes.

three spheres, allowed to have different radii, are proportional to the radii. The velocity of motion can then be calculated using the Stokes-Oseen force-velocity relations, and the ratio of the total driving force and the velocity, appropriately normalized, gives the effective radius of the swimmer. This gives to the first order in r_i/l_j (see SI),

$$\frac{1}{r_{\text{eff}}} = \frac{1}{r_1 + r_2 + r_3} \left\{ 1 + \frac{1}{2} \left[r_1 \left(\frac{1}{l_1} + \frac{1}{l_1 + l_2} \right) + r_2 \left(\frac{1}{l_1} + \frac{1}{l_2} \right) + r_3 \left(\frac{1}{l_1 + l_2} + \frac{1}{l_2} \right) \right] \right\}, \quad (11)$$

where the general form of the expression for unequal r_i 's and l_i 's is presented. Ref. [36] states the effective radius of the three-sphere swimmer for the case of equal $r_i = r$ and $l_i = l$. To the first order in r/l and zeroth order in d_i/l_j , the formula therein agrees with Eq. (11) and gives $r_{\text{eff}} = 6rl/(5r + 2l)$. For our swimmers, with $r = 6.0 \times 10^{-6}$ m and $l = 3.2 \times 10^{-5}$ m, this results in $r_{\text{eff}} = 1.23 \times 10^{-5}$ m.

Intermediate regime for the three-sphere swimmer. As described before, we turn off the driving forces on our swimmer in the steady state, for each simulation marked in Fig. 3, and then compare the relaxation curves to Eqs. (9) and (10). Fig. 4 shows the relaxation obtained from simulation (blue dotted curve) and the fit to this curve using Eq. (9) (orange solid curve) for three different force amplitude values. In each case, the fit parameters are chosen such that they minimise the error to the simulation curve in the initial part of the relaxation, *i.e.* from the initial point on the left to the first local minimum.

The middle simulation in Fig. 4, with a force amplitude of 1.86×10^{-5} N, shows perfect agreement with the theoretically predicted relaxation curve based on Eq. (9), and thus identifies the transition between the Stokes and the non-Stokes regimes. For the smallest force amplitude of 3.71×10^{-6} N (leftmost plot, Fig. 4), the swimmer's motion after the first local minimum is much more damped in the actual simulation (blue dotted) curve than in the fitted (solid orange) curve. In contrast, for the largest force amplitude value of 3.71×10^{-5} N (rightmost plot, Fig. 4), the damping seen in the simulation is weaker than as anticipated by the fitted curve. This behaviour is consistent with the notion of the swimmer's motion going from overdamped to underdamped as the driving forces increase.

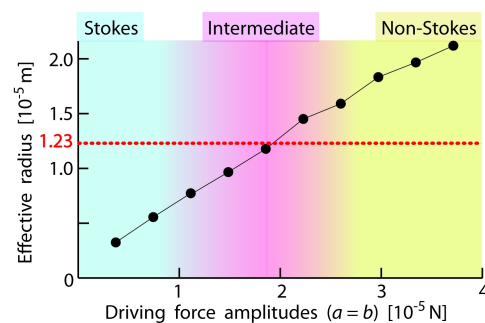


Fig. 5: Effective radius of swimmer for different force amplitudes, as determined by relaxation after force cut-off. Only the simulations in the intermediate regime are expected to reproduce the theoretically predicted value of 1.23×10^{-5} m (marked by a dashed red line).

The determination of the transition regime is confirmed when one uses Eq. (10), with the value of γ found from the fits based on Eq. (9), to calculate the effective radius r_{eff} of the swimmer in each simulation (Fig. 5). The simulation with force amplitudes equalling 1.86×10^{-5} N leads to an r_{eff} value which matches very well the theoretically expected value of 1.23×10^{-5} m. In general, the r_{eff} value found from simulations increases monotonically as the driving forces increase, because the parameter γ found from Eqs. (9) and (10) initially underestimates and then overestimates the actual damping in the simulations.

It is interesting to compare the Reynolds numbers in the different simulations. We measure not just the Reynolds number of the entire swimmer, but also that of the three individual spheres (Table 2 in the SI). These are defined respectively as $Re_{\text{swim}} = u_{\text{swim}} l_{\text{swim}}/\nu$, and $Re^{S_i} = u^{S_i} l^{S_i}/\nu$ (for $i = 1, 2, 3$). Here l_{swim} is the rest length of the swimmer along the direction of motion, equalling 76 lattice cells, u_{swim} is the swimmer's velocity in the last full cycle, u^{S_i} denotes the maximum velocity of the i^{th} sphere during the last cycle and l^{S_i} is a sphere's diameter, equalling 12 lattice cells. We find that the Reynolds numbers increase monotonically with the driving force, and, more interestingly, that they remain small across all the simulations. In particular, for the simulation in the intermediate regime (*i.e.* with force amplitudes 1.86×10^{-5} N) the swimmer Reynolds number is $Re_{\text{swim}} = 0.015$, while

the simulation in the non-Stokes regime (with force amplitudes 3.71×10^{-5} N) has $Re_{\text{swim}} = 0.064$. This shows the narrowness (in terms of the Re value range) of the intermediate regime, and underscores the fact that inertial effects for the swimmer set in at low Reynolds numbers much smaller than 1.

Conclusions. – We have studied the motion of the three-sphere microswimmer when inertial influences on its motion start becoming significant. We have simulated the swimmer under the action of increasing driving forces, using a framework which combines the lattice Boltzmann-based WALBERLA system and the rigid body engine *pe*. By comparing with theory at small values of the Reynolds number (below 10^{-2}) we have shown the suitability of the simulation system for studying the microswimming motion. For increasing Reynolds numbers, the theoretical analysis starts to be inapplicable, as non-Stokesian effects in the motion become visible. In this case we have based our analysis on the simulations, and determined the limits of the Stokes regime by combining the Stokes force law with the expected trajectory of an underdamped harmonic oscillator. The effective hydrodynamic radius of the swimmer obtained in this way agrees excellently with the theoretical value, indicating that the method may be used to determine the effective radius of any mechanical microswimmer driven by elastic shape changes. We have found that the swimmer is in the Stokes regime for $Re \lesssim 10^{-2}$, and in the non-Stokes regime for $Re \gtrsim 5 \times 10^{-2}$. These values are smaller than the often-assumed bound of $Re \leq 1$ for microswimmers, and smaller also than previous estimates in the literature.

* * *

The work was supported by KONWIHR under the project ParSwarm.

REFERENCES

- [1] BERG H. C., *E. coli in Motion* (Springer-Verlag New York) 2004.
- [2] GUASTO J. S., JOHNSON K. A. and GOLLUB J. P., *Phys. Rev. Lett.*, **105** (2010) 168102.
- [3] PURCELL E. M., *Am. J. Phys.*, **45** (1977) 3.
- [4] NAJAFI A. and GOLESTANIAN R., *Phys. Rev. E*, **69** (2004) 062901.
- [5] DREYFUS R., BAUDRY J., ROPER M. L., FERMIGIER M., STONE H. A. and BIBETTE J., *Nature*, **437** (2005) 862.
- [6] AVRON J. E., KENNETH O. and OAKNIN D. H., *New J. Phys.*, **7** (2005) 234.
- [7] BARABAN L., TASINKEVYCH M., POPESCU M. N., SANCHEZ S., DIETRICH S. and SCHMIDT O. G., *Soft Matter*, **8** (2012) 48.
- [8] YEOMANS J., PUSHKIN D. and SHUM H., *Eur. Phys. J. Special Topics*, **223** (2014) 1771.
- [9] HAPPEL J. and BRENNER H., *Low Reynolds Number Hydrodynamics* (Springer Netherlands) 1983.
- [10] KOCH D. L. and SUBRAMANIAN G., *Annu. Rev. Fluid Mech.*, **43** (2011) 637.
- [11] LAUGA E. and POWERS T. R., *Rep. Prog. Phys.*, **72** (2009) 096601.
- [12] ELGETI J., WINKLER R. G. and GOMPPER G., *Rep. Prog. Phys.*, **78** (2015) 056601.
- [13] NGO V. and MCHENRY M. J., *J. Exp. Biol.*, **217** (2014) 72740.
- [14] CHILDRESS S., *Mechanics of swimming and flying* (Cambridge University Press) 1981.
- [15] POOLEY C. M. and YEOMANS J. M., *Comp. Phys. Commun.*, **179** (2008) 159.
- [16] PICKL K., HOFMANN M., PRECLIK T., KÖSTLER H., SMITH A.-S. and RÜDE U., in *Parallel Computing: Accelerating Computational Science and Engineering (CSE)* Vol. 25 of *Advances in Parallel Computing* (IOS Press) 2014 pp. 395–404.
- [17] FEICHTINGER C., DONATH S., KÖSTLER H., GÖTZ J. and RÜDE U., *J. Comput. Sci.*, **2** (2011) 105 .
- [18] FEICHTINGER C., HABICH J., KÖSTLER H., HAGER G., RÜDE U. and WELLEIN G., *Parallel Computing*, **37** (2011) 536 .
- [19] KÖSTLER H. and RÜDE U., *IT - Information Technology*, **55** (2013) 91.
- [20] IGLBERGER K. and RÜDE U., *Multibody Syst. Dyn.*, **25** (2011) 81.
- [21] AIDUN C. K. and CLAUSEN J. R., *Annu. Rev. Fluid Mech.*, **42** (2010) 439.
- [22] SUCCI S., *The Lattice Boltzmann Equation - For Fluid Dynamics and Beyond* (Clarendon Press) 2001.
- [23] QIAN Y. H., D’HUMIÈRES D. and LALLEMAND P., *EPL*, **17** (1992) 479.
- [24] GINZBURG I., VERHAEGHE F. and D’HUMIÈRES D., *Commun. Comput. Phys.*, **3** (2008) 427.
- [25] GODENSCHWAGER C., SCHORNBAUM F., BAUER M., KÖSTLER H. and RÜDE U., in proc. of *Proceedings of the International Conference on High Performance Computing, Networking, Storage, and Analysis SC’13* (ACM) 2013 pp. 35:1–35:12.
- [26] CUNDALL P. A. and STRACK O. D. L., *Géotechnique*, **29** (1979) 47.
- [27] PRECLIK T. and RÜDE U., *Comp. Part. Mech.*, **2** (2015) 173.
- [28] PICKL K., GÖTZ J., IGLBERGER K., PANDE J., MECKE K., SMITH A.-S. and RÜDE U., *J. Comput. Sci.*, **3** (2012) 374.
- [29] GÖTZ J., IGLBERGER K., STÜRMER M. and RÜDE U., in proc. of *Proceedings of the 2010 ACM/IEEE International Conference for High Performance Computing, Networking, Storage and Analysis SC ’10* (IEEE Computer Society) 2010 pp. 1–11.
- [30] LADD A. J. C., *J. Fluid Mech.*, **271** (1994) 285.
- [31] LADD A. J. C., *J. Fluid Mech.*, **271** (1994) 311.
- [32] YU D., MEI R., LUO L.-S. and SHYY W., *Prog. Aerosp. Sci.*, **39** (2003) 329.
- [33] IGLBERGER K., THÜREY N. and RÜDE U., *Comput. Math. Appl.*, **55** (2008) 1461.
- [34] PANDE J., MERCHANT L., KRÜGER T., HARTING J. and SMITH A.-S., *arXiv*, (2014) arXiv:1411.5723.
- [35] PANDE J. and SMITH A.-S., *Soft Matter*, **11** (2015) 2364.
- [36] GOLESTANIAN R. and AJDARI A., *Phys. Rev. E*, **77** (2008) 036308.